The starburst–active galactic nucleus connection in the merger galaxy Mrk 938: an infrared and X-ray view[*]

P. Esquej,[1,2,3]† A. Alonso-Herrero,[1,2]‡ A. M. Pérez-García,[4,5] M. Pereira-Santaella,[1]
D. Rigopoulou,[6] M. Sánchez-Portal,[7] M. Castillo,[7] C. Ramos Almeida,[8] D. Coia,[7]
B. Altieri,[7] J. A. Acosta-Pulido,[4,5] L. Conversi,[7] J. I. González-Serrano,[2]
E. Hatziminaoglou,[9] M. Pović,[10] J. M. Rodríguez-Espinosa[4,5] and I. Valtchanov[7]

[1]*Centro de Astrobiología, INTA-CSIC, E-28850 Madrid, Spain*
[2]*Instituto de Física de Cantabria, CSIC-Universidad de Cantabria, 39005 Santander, Spain*
[3]*Departamento de Física Moderna, Universidad de Cantabria, Avda. de Los Castros s/n, 39005 Santander, Spain*
[4]*Instituto de Astrofísica de Canarias (IAC), C/Vía Láctea, s/n, E-38205 La Laguna, Tenerife, Spain*
[5]*Departamento de Astrofísica, Universidad de La Laguna, E-38205 Tenerife, Spain*
[6]*Astrophysics Department, University of Oxford, Oxford OX1 3RH*
[7]*Herschel Science Centre, ESAC, Apartado 78, 28691 Villanueva de la Cañada, Madrid, Spain*
[8]*Department of Physics and Astronomy, University of Sheffield, Sheffield S3 7RH*
[9]*European Southern Observatory, Karl-Schwarzschild-Str. 2, 85748 Garching bei München, Germany*
[10]*Instituto de Astrofísica de Andalucía (CSIC), Apdo. 3004, 18080 Granada, Spain*

ABSTRACT

Mrk 938 is a luminous infrared (IR) galaxy in the local Universe believed to be the remnant of a galaxy merger. It shows a Seyfert 2 nucleus and intense star formation according to optical spectroscopic observations. We have studied this galaxy using new *Herschel* far-IR imaging data in addition to archival X-ray, UV, optical, near-IR and mid-IR data. Mid- and far-IR data are crucial to characterize the starburst contribution, allowing us to shed new light on its nature and to study the coexistence of active galactic nuclei (AGN) and starburst activity in the local Universe. The decomposition of the mid-IR *Spitzer* spectrum shows that the AGN bolometric contribution to the mid-IR and total IR luminosity is small [$L_{bol}(AGN)/L_{IR} \sim 0.02$], which agrees with previous estimations. We have characterized the physical nature of its strong IR emission and constrained it to a relatively compact emitting region of ≤ 2 kpc. It is in this obscured region where most of the current star formation activity is taking place as expected for luminous IR galaxies. We have used *Herschel* imaging data for the first time to constrain the cold dust emission with unprecedented accuracy. We have fitted the integrated far-IR spectral energy distribution and derived the properties of the dust, obtaining a dust mass of $3 \times 10^7\,M_\odot$. The far-IR is dominated by emission at 35 K, consistent with dust heated by the ongoing star formation activity.

Key words: galaxies: evolution – galaxies: individual: Mrk938 – galaxies: nuclei – galaxies: Seyfert – galaxies: structure – infrared: galaxies.

1 INTRODUCTION

Observations over the past decade have revealed that supermassive black holes (SMBHs) likely reside at the centres of all galaxies with

---

[*] *Herschel* is an ESA space observatory with science instruments provided by European-led Principal Investigator consortia and with important participation from NASA.
†E-mail: pilar.esquej@cab.inta-csic.es
‡Augusto González Linares Senior Research Fellow.

spheroids (see Kormendy & Richstone 1995, for a review) and that the properties of these black holes and their host galaxies are tightly correlated (e.g. Marconi & Hunt 2003; Ferrarese & Ford 2005). In addition, the similarity in the anti-hierarchical evolution of both star formation rate (SFR) and active galactic nuclei (AGN) activity at $z < 2$ (La Franca et al. 2005; Arnouts et al. 2007) reveals that the assembly and evolution of galaxies and the SMBHs at their centres are intimately connected. However, the nature of such an intrinsic connection is still enigmatic. Since it is believed that the main phase of SMBH growth through major mergers occurs in environments heavily obscured by dust (Hopkins et al. 2006), the infrared (IR)

domain is the path to follow to unveil key signatures that remain lurking at other wavelengths.

The class of objects known as luminous IR galaxies (LIRGs; $L_{IR} = 10^{11}$–10^{12} L$_\odot$, IR in the range 8–1000 μm) contributes a significant fraction (≥50 per cent) of the cosmic IR background. In addition, they are major contributors to the star formation activity at $z \sim 1$ (Elbaz et al. 2002; Le Floc'h et al. 2005; Pérez-González et al. 2005). LIRGs are powered by star formation and/or AGN activity, and a large fraction of them, especially at the high IR luminosity end, are classified as interacting galaxies and mergers (Sanders & Mirabel 1996). It has been suggested that the mechanisms that trigger mass accretion on to the SMBH through major merger processes are episodes of nuclear star formation (Hopkins et al. 2006). Therefore, it is clear that studying LIRGs can shed new light on our understanding of the coeval evolution of host galaxy and black hole.

Mrk 938 (also known as NGC 34, NGC 17 and IRAS F00085−1223, among others) is a local LIRG belonging to the *IRAS* Revised Bright Galaxy Sample (Sanders et al. 2003) – RA = $00^h11^m06\overset{s}{.}65$, Dec. = $-12°06^m26\overset{.}{.}7$. It is located at a distance of 86.4 Mpc using the recession velocity relative to the Local Group $cz_{LG} = 5961$ km s^{-1} measured by Schweizer & Seitzer (2007) and assuming a Λ cold dark matter (ΛCDM) cosmology with (Ω_M, Ω_Λ) = (0.3, 0.7) and $H_0 = 70$ km s^{-1} Mpc^{-1}. The measured IR luminosity of this galaxy is $L_{IR} = 3.4 \times 10^{11}$ L$_\odot$ using the *IRAS* fluxes reported by Sanders et al. (2003) and the adopted distance. Although this source has been classified in the literature as both Seyfert 2 and starburst (SB) galaxy from optical spectroscopy (see Schweizer & Seitzer 2007, for a detailed discussion on this issue), its X-ray emission confirms the presence of an obscured AGN (see Guainazzi, Matt & Perola 2005, and also Section 3.1). We note that in the recent work of Yuan, Kewley & Sanders (2010) the nuclear activity of Mrk 938 has been definitively classified as Seyfert 2 based on optical spectroscopy.

The optical morphology of Mrk 938 is dominated by a bright red nucleus, a blue exponential disc, and a rich system of young massive star clusters. The faint optical surface brightness emission reveals a pair of tidal tails to the north-east and south-west of the system, with the former being the brightest and longest one (see Fig. 1, courtesy of F. Schweizer). All these signatures led Schweizer & Seitzer (2007) to propose that Mrk 938 is the remnant of a gas-rich merger of two unequal mass galaxies. The nuclei of the two galaxies have probably coalesced, creating a concentrated and obscured SB and an AGN, both driving a strong gaseous outflow. The SB appears to be confined to a highly obscured central region of less than 1 kpc in radius (Schweizer & Seitzer 2007). This is indeed confirmed by ground-based high-angular resolution observations in the mid-IR. These revealed that the mid-IR emission in this system originates in the central ∼800 pc (Miles et al. 1996), but it actually dominates in a region of ∼400 pc (see discussion in Section 4.1). Fernández et al. (2010) detected H I emission from both tidal tails and from nearby galaxies, suggesting that Mrk 938 is part of a gas-rich group of galaxies. They also found a hint of emission between Mrk 938 and NGC 35, the largest companion lying at a projected distance of 131 kpc, and suggested that they might have recently interacted. The radio-continuum emission detected in the nuclear region is extended, indicating that it is mostly due to the highly concentrated SB.

Here we present for the first time a detailed analysis of novel far-IR (70–500 μm) imaging observations of Mrk 938 obtained with the *Herschel Infrared Observatory* (Pilbratt et al. 2010). These have been combined with our own analysis of X-ray, UV and IR data
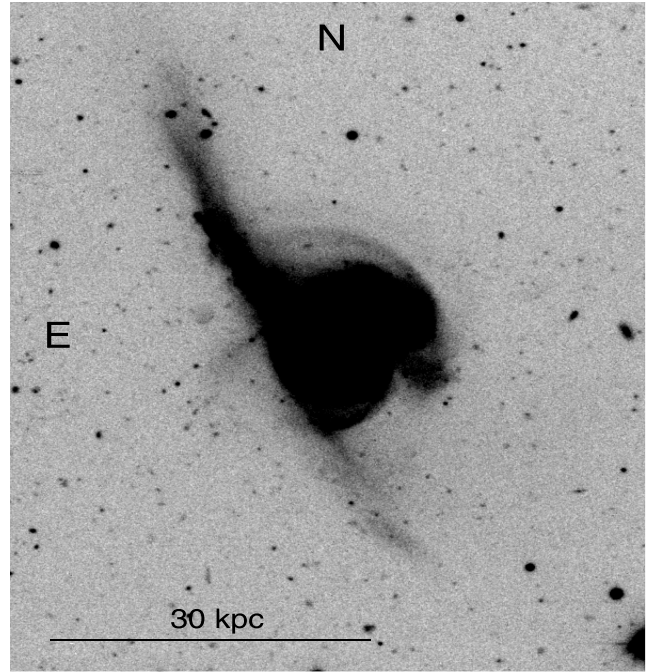

Figure 1. Ground-based 2.5 × 3 arcmin² *B*-band image of Mrk 938 provided by F. Schweizer. Note the bright nucleus and spiral structure in addition to the two tidal tails emerging from the system in opposite directions.

already presented in the literature. The main goal of this work is to understand the AGN/SB connection in Mrk 938, as well as the origin of the IR emission of this galaxy. This is the second paper in a series presenting *Herschel* imaging observations of a sample of nearby Seyfert galaxies to investigate the coexistence of AGN and SB activity, as well as the nature of the dusty torus. A study of the dust properties of NGC 3081 has recently been presented in Ramos Almeida et al. (2011b).

This paper is structured as follows. Section 2 describes the data analysis procedure of the different IR and X-ray observations. In Section 3 we present evidence of AGN activity, including the decomposition of the mid-IR spectrum into AGN and SB contributions. The properties of the SB component have been derived in Section 4. We used the wealth of archival data to fit the spectral energy distribution (SED) of the galaxy and to derive the dust properties, presented in Section 5. Finally, our findings and conclusions are summarized in Section 6.

2 OBSERVATIONS AND DATA ANALYSIS

2.1 *Herschel*

We performed far-IR imaging observations of Mrk 938 with the Photodetector Array Camera and Spectrometer (PACS; Poglitsch et al. 2010) and the Spectral and Photometric Imaging REceiver (SPIRE; Griffin et al. 2010) on-board the *Herschel Space Observatory* (Pilbratt et al. 2010), covering the spectral range 70–500 μm in six bands. The data are part of the guaranteed time proposal 'Herschel imaging photometry of nearby Seyfert galaxies: testing the coexistence of AGN and SB activity and the nature of the dusty torus' (PI: M. Sánchez-Portal).

The PACS observations were carried out using the 'mini-map' mode, consisting of two concatenated scan line maps, at 70° and 110° (in array coordinates), at a speed of 20 arcsec s^{-1}, each one
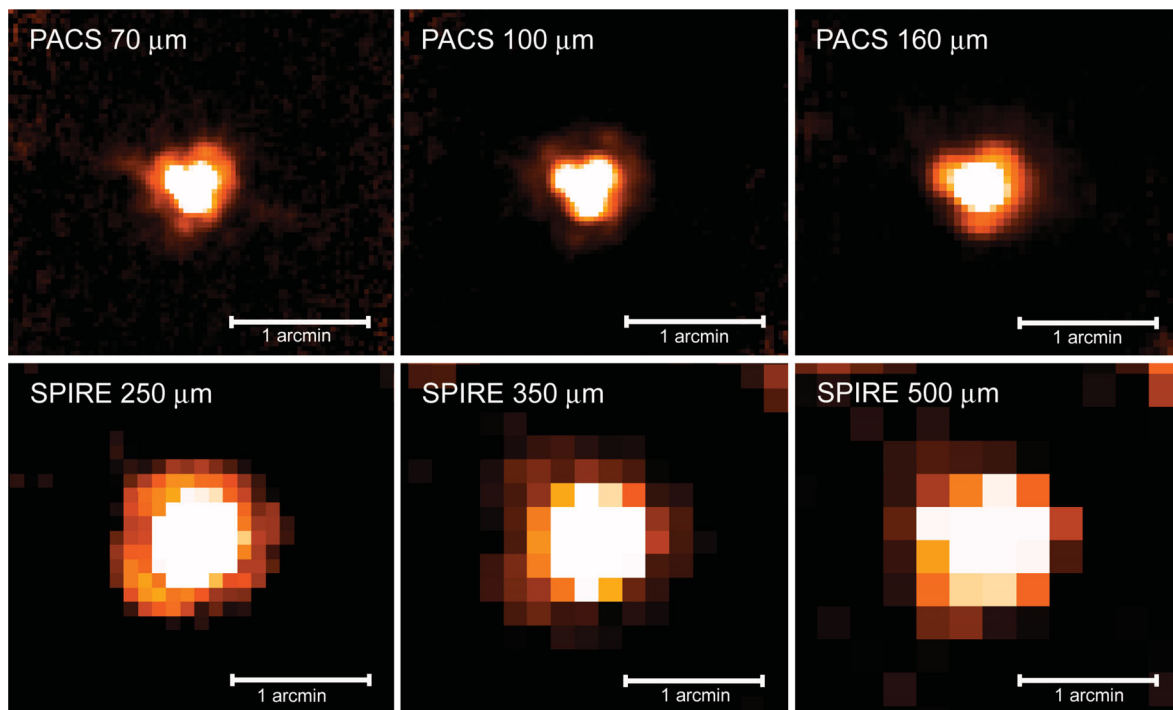
Figure 2. *Herschel* images of 3×3 arcmin^2 centred on Mrk 938. North/east is up/left, respectively. Top: PACS 70, 100 and 160 μm; bottom: SPIRE 250, 350 and 500 μm; from left to right, respectively. The PACS images show the shape of the point spread function (PSF). In particular, a plume-like structure lying approximately in the NE–SW direction has been deemed as a PSF artefact and it should not be confused with the tidal tail observed in the IRAC images (Fig. 3).

with 10 lines of 3 arcmin length and cross-scan step of 4 arcsec. This mode produces a highly homogeneous exposure map within the central 1-arcmin area. The set of maps was duplicated to observe through both the 70-μm ('blue') and 100-μm ('green') filters. Therefore, the galaxy was observed twice through the 160-μm ('red') filter. The PACS beams at 70, 100 and 160 μm are 5.6, 6.8 and 11.3 arcsec full width at half-maximum (FWHM), respectively. With the SPIRE photometer, the three available bands were observed simultaneously using the 'small map' mode, with two 1×1 nearly orthogonal scan lines, at a scan speed of 30 arcsec s^{-1}. The scan line length is 11.3 arcmin and the area for scientific use is around 5×5 arcmin^2. The FWHM beam sizes at 250, 350 and 500 μm are 18.1, 25.2 and 36.9 arcsec, respectively.

The data reduction was carried out with the *Herschel* Interactive Processing Environment (HIPE) v6.0.1951. For the PACS instrument, the extended source version of the standard `PhotProject` reduction script was deemed as adequate, due to the small angular size of the galaxy. This procedure implements a high-pass filtering algorithm to remove the 1/*f* noise of the bolometer signals. The sources are masked in order to prevent the high-pass filter to remove flux from extended structures. The Flight Model (FM) v5 photometer response calibration files (Müller et al. 2011) were used. Level 2 maps produced by the reduction script for the two scan directions were merged using the `mosaic` task. For SPIRE, the standard small map script with the 'naïve' scan mapper task was applied, using the calibration data base v6.1. Colour corrections (for PACS, see Poglitsch et al. 2010; for SPIRE, please refer to the *Observer's Manual*) are small for blackbodies at the expected temperatures (e.g. Pérez García & Rodríguez Espinosa 2001) and have been neglected. More details on the processing of *Herschel* data are given in Sánchez-Portal et al. (in preparation). The far-IR maps of Mrk 938 are shown in Fig. 2.

Aperture photometric data in the different bands were extracted using IRAF[1] and the measurements for an aperture radius of 70 arcsec are shown in Table 1. The selected radius is a good compromise between including all IR emission and minimizing the background contribution. Since the PACS encircled energy radius of FM v5 is normalized to an aperture of 60 arcsec, no aperture correction for the data was required. The morphology of Mrk 938, which will be further discussed in Section 4.1, is compatible with an unresolved object. Using our far-IR and $L_{24\,\mu m}$ photometry and the parametrization of Dale & Helou (2002), we derived a total IR luminosity of $L_{IR} = 3.3 \times 10^{11}\,L_\odot$, in agreement with that of Sanders et al. (2003).

2.2 *Spitzer*

2.2.1 *Imaging Observations*

Mrk 938 was observed with the *Spitzer* instruments Infrared Array Camera (IRAC) (Fazio et al. 2004) and Multiband Imaging Photometer for *Spitzer* (MIPS) (Rieke et al. 2004). We retrieved the basic calibrated data (BCD) from the *Spitzer* archive (IRAC – P3269, PI: J.F. Gallimore; MIPS – P3672, PI: J.M. Mazzarella). The BCD processing includes corrections for the instrumental response (e.g. pixel response linearization), flagging of cosmic rays and saturated pixels, dark and flat-fielding corrections, and flux calibration based on standard stars (see the IRAC and MIPS instrument handbooks for details). We combined the BCD images into mosaics using the

---

[1] Image Reduction and Analysis Facility (IRAF) software is distributed by the National Optical Astronomy Observatories, which is operated by the Association of Universities for Research in Astronomy, Inc., under cooperative agreement with the National Science Foundation.

Table 1. Integrated IR SED of Mrk 938.

Name	λ (μm)	f_ν (Jy)	Error (Jy)	Reference
2MASS	1.2	0.051	0.001	Jarrett et al. (2003)
2MASS	1.6	0.067	0.002	Jarrett et al. (2003)
2MASS	2.2	0.062	0.002	Jarrett et al. (2003)
Spitzer-IRAC	3.6	0.043	0.002	Gallimore et al. (2010)
Spitzer-IRAC	4.5	0.036	0.001	Gallimore et al. (2010)
Spitzer-IRAC	5.8	0.092	0.004	Gallimore et al. (2010)
Spitzer-IRAC	8.0	0.59	0.01	Gallimore et al. (2010)
IRAS	12	0.35	0.032	Sanders et al. (2003)
Spitzer-IRS	15	0.435	0.012	Deo et al. (2007)
Spitzer-MIPS	24	1.84	0.18	This work
IRAS	25	2.39	0.055	Sanders et al. (2003)
Spitzer-IRS	30	4.36	0.05	Deo et al. (2007)
IRAS	60	17.05	0.045	Sanders et al. (2003)
Herschel-PACS	70	14.80	1.48	This work
IRAS	100	16.86	0.135	Sanders et al. (2003)
Herschel-PACS	100	15.00	1.50	This work
ISO-ISOPHOT	120	17.20	0.40	Spinoglio, Andreani & Malkan (2002)
ISO-ISOPHOT	150	10.60	0.50	Spinoglio, Andreani & Malkan (2002)
Herschel-PACS	160	8.90	0.89	This work
ISO-ISOPHOT	170	8.50	0.20	Spinoglio et al. (2002)
ISO-ISOPHOT	180	5.40	0.10	Spinoglio et al. (2002)
ISO-ISOPHOT	200	3.00	0.10	Spinoglio et al. (2002)
Herschel-SPIRE	250	2.80	0.28	This work
Herschel-SPIRE	350	0.90	0.09	This work
Herschel-SPIRE	500	0.20	0.02	This work
IRAM-30 m	1300	0.0097	0.0018	Albrecht, Krügel & Chini (2007)

MOsaicker and Point source EXtractor (MOPEX) software provided by the *Spitzer* Science Center (SSC) using the standard parameters. IRAC images of Mrk 938 at 3.6 and 8 μm are shown in Fig. 3. The IRAC 8-μm image was affected by the banding effect (see IRAC Handbook). Similar to Gallimore et al. (2010), we corrected this artefact by fitting a polynomial to the affected rows.

We computed integrated photometry of the source in the MIPS 24-μm image, and obtained from the literature photometric data points for the IRAC bands (Gallimore et al. 2010). The source photometry is presented in Table 1.

2.2.2 Spectroscopic observations

We retrieved *Spitzer*/Infrared Spectrograph (IRS) (Houck et al. 2004) spectroscopic observations of Mrk 938 from the *Spitzer* archive (P3269, PI: J.F. Gallimore; P30291, PI: G. Fazio). The observations were taken in low-resolution ($R \sim$ 60–120) with the Short-Low (SL) and Long-Low (LL) modules and in high-resolution ($R \sim$ 600) mode with the Short-High (SH) and Long-High (LH) modules. The low-resolution data were observed in mapping mode while the high-resolution data were obtained in staring mode.

For the staring data we started with the BCD data. Bad pixels were corrected using the IDL package IRSCLEAN.[2] Then we subtracted the sky emission and extracted the spectra using the standard programs included in the *Spitzer* IRS Custom Extraction (SPICE) package provided by the SSC and the point source calibration. The resulting

spectrum was already presented in Tommasin et al. (2010). For the SL+LL mapping observations, we constructed the data cubes using CUBISM (Smith et al. 2007). We extracted the nuclear spectrum of Mrk 938 observed in SL+LL mapping mode using a 13.4 × 13.4 arcsec^2 aperture. Since the mapping mode data cubes are calibrated as extended sources, we applied a wavelength-dependent aperture correction to obtain a point-like spectrum to represent the nuclear emission of this galaxy. For more details on the data analysis, please see Pereira-Santaella et al. (2010a,b); Alonso-Herrero et al. (2012).

We evaluated the strength of the 9.7-μm silicate feature, S_{Si}, by calculating the ratio of the observed flux density to the continuum flux density at 9.7 μm using the method in Pereira-Santaella et al. (2010b). Applying the definition of Spoon et al. (2007), we get $S_{Si} = -1.1$, where the minus sign indicates absorption. This value is considerably higher, in absolute terms, than the average of the LIRG sample in Alonso-Herrero et al. (2012) of $\langle S_{Si} \rangle = -0.6$. We also measured the equivalent width (EW) of the 6.2-μm polycyclic aromatic hydrocarbon (PAH) feature, and obtained EW(PAH 6.2 μm) = 0.4±0.1 μm. Spoon et al. (2007) provided a diagnostic diagram to give a general classification of IR galaxies based on S_{Si} and EW(PAH 6.2 μm). According to that, Mrk 938 is a moderately obscured composite nucleus.

2.3 XMM–Newton

Mrk 938 was observed by *XMM–Newton* on 2002 December 22 (rev 556, obsid 0150480501, PI: R. Maiolino) and then analysed with the *XMM–Newton* Science Analysis Software (SAS; Gabriel et al. 2004). All European Photon Imaging Camera (EPIC) observations

---

[2] The IRSCLEAN package is available at http://irsa.ipac.caltech.edu/data/SPITZER/docs/dataanalysistools/tools/irsclean/.
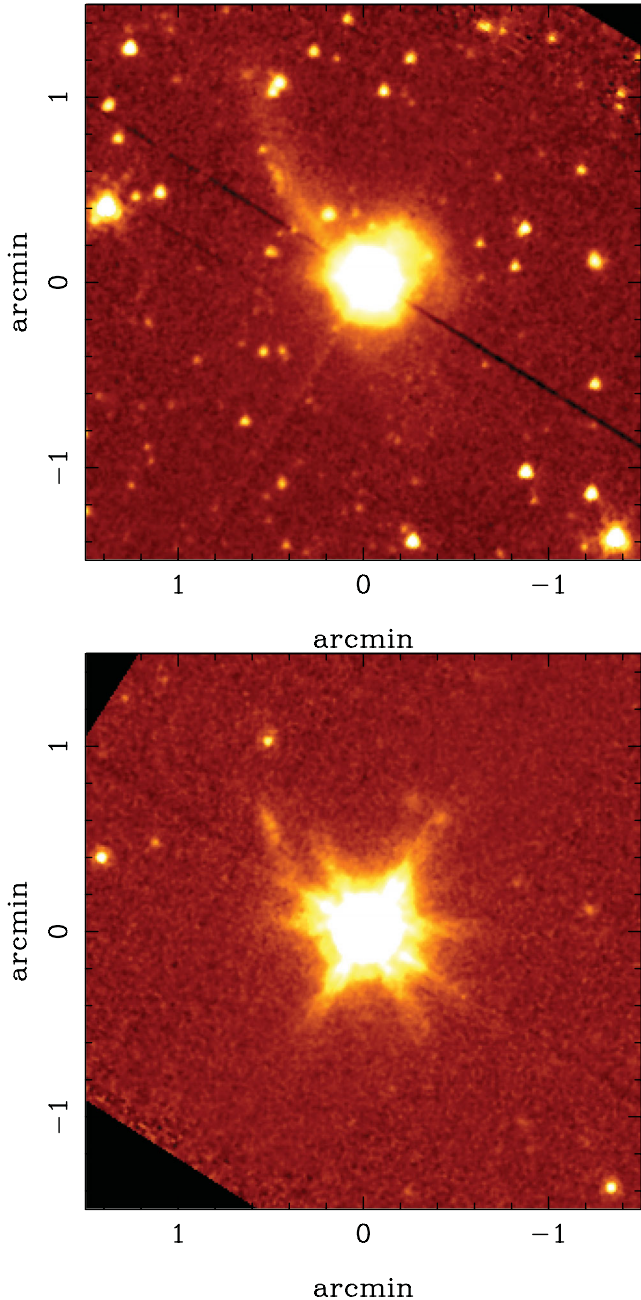
Figure 3. *Spitzer*/IRAC images at 3.6 (top) and 8 μm (bottom) of Mrk 938 covering a field of view of 3 × 3 arcmin². The orientation is north up, east to the left. Images are shown in a square root scale. Note that the north-east tidal tail and knots of star formation are clearly detected in the 3.6-μm image, which traces photospheric emission. In the 8-μm image, which probes dust continuum and PAH emission, one can see faint emission in that tail likely to be associated with the knots of star formation also seen in the optical (see Fig. 1).

were taken in full frame mode and the medium filter in place. These data were already presented in Guainazzi et al. (2005), but we reduced them with the latest software to take full advantage of the most recent calibration files.

To extract the X-ray spectra, high background periods produced by intense soft proton fluxes were rejected by defining good time intervals within the complete observation window. After this process, the net exposure times were about 13, 16 and 16 ks for pn,

MOS1 and MOS2, respectively. The light curves of the sources were inspected and no variability within the X-ray observations was observed. Source photons were extracted from a circular region of 30-arcsec radius centred on the object position. A circular source-free region on the same chip and radius of 60 arcsec were used to characterize the background. The target does not suffer from pile-up, so the pn spectrum was extracted with patterns 0–4, and MOS spectra from 0 to 12. Ancillary files and response matrices were generated by the `arfgen` and `rmfgen` SAS tasks respectively in order to convert the counts to physical units during the spectral analysis. All EPIC spectra were binned to oversample the instrumental resolution and to have no less than 20 counts in each background-subtracted spectral channel.

Spectral fitting was performed with XSPEC 12, where all applied models include Galactic foreground absorption ($N_H = 2.61 \times 10^{20}$ cm^{-2}) inferred from H I observations (Dickey & Lockman 1990). Given that our source has been found to be highly obscured, we started fitting the data with a model consisting of a power law plus an absorbed power law, both with the same photon index. We got a reasonable fit at high energies, but a prominent soft excess with respect to the power law appeared below ∼1 keV. Thus we added a thermal component, `MEKAL` in XSPEC. We obtained a temperature $kT = 0.67$ keV typical of a SB emission, and a high intrinsic absorption of $N_H^{int} = 75^{+31}_{-21} \times 10^{22}$ cm^{-2}, consistent with high obscuration. A considerably flat power law was obtained, $\Gamma_X = 1.43$. A summary of the parameters of this model, which is considered our best fit (χ^2/d.o.f. = 50/64), is presented in Table 2. Our derived X-ray luminosity is similar to that in Guainazzi et al. (2005). Fig. 4 shows the X-ray data (only EPIC-pn data are shown for simplicity) and model-to-data residuals. We also tried adding a reflection model (`PEXRAV`, Magdziarz & Zdziarski 1995), for possible X-ray

Table 2. Parameters derived from the fitting of the best-fitting model, zwabs×(mekal+zpo+zwabs×zpo) in XSPEC nomenclature, to the *XMM–Newton* data. Galactic foreground absorption has been used for the first model component. Errors are 90 per cent confidence.

kT (keV)	N_H^{int} (10^{22} cm^{-2})	Γ_X	$L_{0.5-2\,keV}$[a] (10^{40} erg s^{-1})	$L_{2-10\,keV}$[b] (10^{42} erg s^{-1})
$0.67^{+0.08}_{-0.07}$	75^{+31}_{-21}	$1.43^{+0.24}_{-0.26}$	$5.4^{+0.9}_{-0.8}$	$1.4^{+0.3}_{-0.2}$

[a] Luminosity corrected for Galactic absorption
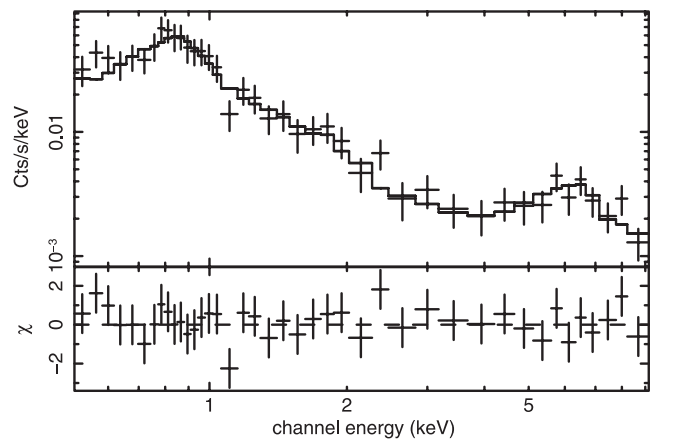[b] Luminosity corrected for Galactic and intrinsic absorption

Figure 4. X-ray spectrum of the EPIC-pn data. The upper panel shows data and best-fitting model (solid line). Residuals in terms of σ values are plotted in the bottom panel.

scattering from an optically thick surface, but did not get any statistical improvement in the fit.

2.4 *Swift*

The position of Mrk 938 has been observed with the Burst Alert Telescope (BAT; Barthelmy et al. 2005), but the source is not detected even in the 70th month survey. We have used the standard BAT tool `batcelldetect`[3] to analyse the observations and derive the rate (normalized by the number of working detectors) at the source position in the eight standard channels from corresponding background subtracted images. In the fourth channel, 35–50 keV, the rate becomes negative, therefore we have combined the first three channels to get a rate in the 14–35 keV energy range. Using WEBPIMMS[4] for the count rate to flux conversion, we get a flux upper limit of 2.5×10^{-12} erg s^{-1} cm^{-2} (equivalent to a luminosity of 2.2×10^{42} erg s^{-1}). If we extrapolate our best-fitting model derived for the *XMM–Newton* data, we get $F_{14-35\,\mathrm{keV}} = 1.6^{+0.8}_{-0.4} \times 10^{-12}$ erg s^{-1} cm^{-2} ($L_{14-35\,\mathrm{keV}} = 1.4^{+0.9}_{-0.5} \times 10^{42}$ erg s^{-1}), which is compatible with a BAT non-detection. We cannot further constrain the X-ray model because the extrapolated fluxes for all reasonable models lie below the BAT upper limit.

3 AGN ACTIVITY

In the local Universe, a significant fraction of LIRGs hosts an AGN, and this fraction increases with the IR luminosity of the system (Veilleux et al. 1995). Using optical emission-line ratios and a new scheme to classify galaxies, Yuan et al. (2010) recently reported that approximately half of local LIRGs are classified as Seyfert, LINER (low ionisation nuclear emission-line region) or composite (SB/AGN). The AGN detection rate in LIRGs can be as high as ∼60 per cent when combining optical and IR indicators (i.e. emission line ratio diagnostics and spectral decomposition; Alonso-Herrero et al. 2012), and thus similar to that of local ultraluminous IR galaxies (ULIRGs; $L_{\mathrm{IR}} = 10^{12}$–$10^{13}$ $L_\odot$; Nardini et al. 2010). However, in clear contrast with ULIRGs, in local LIRGs the AGN bolometric contribution to the IR luminosity of these systems is very small, with an average of $\langle L_{\mathrm{bol}}(\mathrm{AGN})/L_{\mathrm{IR}} \rangle = 0.05^{+0.07}_{-0.03}$ (Alonso-Herrero et al. 2012). Therefore, the high IR luminosities in most LIRGs are produced in intense dusty SBs. Petric et al. (2011) estimated that AGN contribute ∼12 per cent to the IR luminosity, which is compatible with the upper end found in Alonso-Herrero et al. (2012).

3.1 X-ray evidence

The analysis of the X-ray emission of Mrk 938 shows evidence of the presence of an obscured AGN. The active nucleus dominates the hard X-ray contribution as can be seen from the highly absorbed power-law component used to fit the spectrum. The measured absorption-corrected hard X-ray luminosity of $1.4^{+0.3}_{-0.2} \times 10^{42}$ erg s^{-1} is too high to be originated in a pure SB (see Section 4.3). The high intrinsic absorbing column returned by the spectral fitting supports the conclusion of the highly obscured nucleus.

A powerful diagnostic to estimate the nuclear obscuration is the 2–10 keV to [O III] flux ratio, T (e.g. Maiolino et al. 1998; Bassani et al. 1999; Guainazzi et al. 2005). According to previous studies, the

threshold lies in $T = 0.1$, where objects with $T \leq 0.1$ are Compton-thick while those with $T \geq 1$ are unobscured or Compton-thin. Using $F_{\mathrm{[O\,III]}} = 1.1 \times 10^{-14}$ erg s^{-1} cm^{-2} as presented in Polletta et al. (1996), we obtain $T = 0.01$ for our source, therefore Mrk 938 would appear as Compton-thick. However, this galaxy has a very strong SB contribution in the optical (Gonçalves, Véron-Cetty & Véron 1999); therefore, the AGN is not responsible for a considerable fraction of the [O III] flux and the T ratio as a measure of obscuration is uncertain. Another indicator of the nuclear obscuration is the emission fluorescence Fe K$_\alpha$ line. Objects are considered as Compton-thick when EW(Fe K$_\alpha$) > 1000 eV (Matt, Brandt & Fabian 1996). In the case of Mrk 938, due to low statistics at the hardest energies, we can only constrain the presence of the Fe K$_\alpha$ line by extracting an upper limit. Using Cash statistics, Guainazzi et al. (2005) fitted the unbinned spectrum in the 5.25–7.25 keV range. They found an EW upper limit of 322 eV when fitting a Gaussian with energy fixed at 6.4 keV. Therefore, the width of the Fe K$_\alpha$ line places the source in the Compton-thin region.

3.2 Mid-IR evidence

In terms of continuum emission, the mid-IR spectral range contains a wealth of information to disentangle the AGN from the SB contribution in galaxies. This comes from both broad features and fine structure emission lines. In particular, high-metallicity SB galaxies show very similar mid-IR spectra (see e.g. Brandl et al. 2006; Bernard-Salas et al. 2009), which are rather different from the continuum and line emission observed in pure AGN. Because of this, spectral decomposition of *Spitzer*-IRS spectra is a powerful tool to estimate the fractional AGN and SB contributions at different mid-IR wavelengths in both local (see e.g. Nardini et al. 2008, 2010; Alonso-Herrero et al. 2012) and high-*z* (e.g. Menéndez-Delmestre et al. 2009) galaxies.

In the case of local LIRGs, Alonso-Herrero et al. (2012) demonstrated that the mid-IR spectral decomposition can identify even subtle AGN emission that may otherwise be under the detection threshold with other mid-IR diagnostics. Here we used a spectral decomposition method very similar to theirs to estimate the AGN contribution with respect to the total mid-IR emission of Mrk 938. For the SB component this method uses the average SB spectrum of Brandl et al. (2006), and the templates of purely star-forming (U)LIRGs of Rieke et al. (2009) covering the IR luminosity range $10.5 \leq \log (L_{\mathrm{IR}}/L_\odot) \leq 12$. The AGN continuum emission is represented by that produced by an interpolated version of the CLUMPY torus models of Nenkova et al. (2008a, 2008b). We restricted the large data base of the CLUMPY torus models to only use two AGN templates. These were derived by Ramos Almeida et al. (2011a) as the best-fitting models to the average SEDs of nearby type 1 and type 2 Seyferts using a Bayesian code (Asensio Ramos & Ramos Almeida 2009). We then looked for the best combination of SB+AGN templates to fit the IRS spectrum that minimized χ^2. The best fit to the IRS spectrum of Mrk 938 was achieved with the type 2 AGN template, as expected, plus the 10^{12} L$_\odot$ SB template. This SB template is required to fit the relatively deep 9.7-μm silicate feature observed in this galaxy. We note that the IR luminosity of the best-fitting template is higher than that of our galaxy. This might indicate that the IR emission comes from a relatively compact region (Section 4.1), as is the case of many LIRGs.

In Fig. 5 we show the IRS spectrum of Mrk 938 plus the AGN+SB best-fitting model, in addition to the scaled model components. As can be seen from the figure, the AGN contribution to the mid-IR emission is small but detectable. The AGN fractional contributions
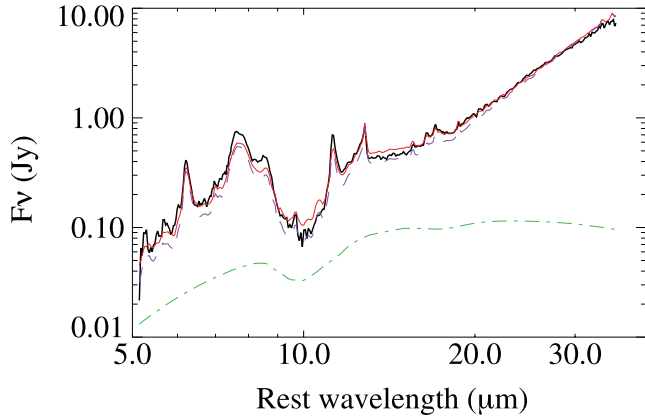
---

[3] http://heasarc.gsfc.nasa.gov/ftools/caldb/help/batcelldetect.html
[4] http://heasarc.nasa.gov/Tools/w3pimms.html

Figure 5. AGN+SB best fit of the observed SL+LL IRS spectrum of Mrk 938 (black line). The dot–dashed green line is the fitted scaled Seyfert 2 torus model template (see text for details), the purple dashed line is the fitted scaled SB template, and the solid red line is the sum of the fitted SB and AGN components.

Table 3. AGN fractional contributions within the IRS slit obtained from the AGN+SB decomposition.

$C_{6\,\mu m}^{IRS}(AGN)$	$C_{20\,\mu m}^{IRS}(AGN)$	$C_{24\,\mu m}^{IRS}(AGN)$	$C_{30\,\mu m}^{IRS}(AGN)$
0.21	0.10	0.05	0.02

to the continuum emission within the *Spitzer*/IRS slit are listed in Table 3. Although our statistical uncertainties on the derived parameters are small (± 5 per cent), the errors associated with the templates can be larger, especially in the SB component. Our results are in good agreement with those of Deo et al. (2009). Clearly, as found in local LIRGs and many local Seyfert galaxies, the AGN contribution at wavelengths longer than 40 μm is greatly reduced (see Mullaney et al. 2011; Alonso-Herrero et al. 2012). Vega et al. (2008) obtained a contribution of 17 per cent of the AGN to the 3–30 μm luminosity, which is at the upper end of the AGN contribution that we find at 20 μm including uncertainties. Tommasin et al. (2010) find an AGN contribution to the 19-μm flux of Mrk 938 of 50 ($\pm$13) per cent, which is considerably higher than our estimation. This can be explained because they used upper limits on the undetected line widths for their estimation.

Additionally, we can use mid-IR high-excitation emission lines to investigate the AGN emission, in particular, the [Ne v] lines at 14.32 and 24.32 μm and the [O iv] λ25.89 μm line (Genzel et al. 1998). Tommasin et al. (2010) did not detect any of these emission lines in Mrk 938 (see also Gallimore et al. 2010; Pereira-Santaella et al. 2010a). When these high-excitation emission lines are ratioed with a line mostly produced by star formation (e.g. the [Ne ii] λ12.81 μm), it is possible to obtain an approximate contribution – if any – of the AGN to the mid-IR emission of a galaxy. The upper limit to the [O iv] λ25.89 μm/[Ne ii] λ12.81 μm of ∼0.01 (Pereira-Santaella et al. 2010a; Tommasin et al. 2010) indicates that the mid-IR emission of this galaxy is dominated by star formation activity (see e.g. Petric et al. 2011; Alonso-Herrero et al. 2012). This is in good agreement with the low AGN fractional contribution to the mid-IR emission inferred from the spectral decomposition.

Since the IRS slit encloses most of the 24-μm emission (from the comparison with the MIPS photometry; see Table 1), the derived AGN fraction contribution to the 24-μm emission is 0.05. Alonso-Herrero et al. (2012) also found that in local LIRGs this fractional

AGN contribution is related to the AGN bolometric contribution to the IR luminosity of the system. Using their relation we estimated that in Mrk 938 $L_{bol}(AGN)/L_{IR} = 0.02^{+0.02}_{-0.01}$. This is in good agreement with the AGN bolometric contribution estimated by Vega et al. (2008) of 4 per cent from their modelling of the full SED of this galaxy. We derived then an AGN bolometric luminosity of $2.6^{+2.6}_{-1.3} \times 10^{43}$ erg s^{-1}. Alternatively, the AGN bolometric luminosity can be estimated from the hard X-ray 2–10 keV luminosity. Using the bolometric correction of Marconi et al. (2004) and our derived X-ray luminosity from the model fit $L_{2-10\,keV} = 1.4 \times 10^{42}$ erg s^{-1} (Table 2), we get a bolometric luminosity of $L_{bol}(AGN) = 1.6^{+1.1}_{-0.6} \times 10^{43}$ erg s^{-1}, compatible with our previous estimation derived from the IRS spectral decomposition.

4 STARBURST ACTIVITY

It is now becoming clear that the size of star-forming regions and the resulting IR surface brightness (also referred as compactness) of IR bright galaxies may help us understanding how star formation is produced in galaxies. This implies that we may be able to differentiate between extended steady star formation in discs and compact star formation activity driven by mergers. These two processes produce different overall IR SEDs of LIRGs and ULIRGs both locally and at high redshift (see e.g. Rujopakarn et al. 2011a,b, and references therein), where there is no clear dependence of the shape of SED with L_{IR}.

Similar to the fundamental planes of spiral and elliptical galaxies, there are three parameters that define a Fundamental Plane of IR-selected galaxies (Chanial et al. 2007). These are the IR luminosity, the dust temperature and the size of the IR-emitting regions. According to these authors, changes in the IR compactness describe a smooth sequence going from quiescent to SB galaxies, where there is a simultaneous increase of gas surface density, effective dust temperature and SFR surface density. In the following sections, we explore in detail some of these properties in Mrk 938.

4.1 IR-emitting region

The detailed study of the optical properties of Mrk 938 (morphology, star cluster ages and dynamics) led Schweizer & Seitzer (2007) to claim that this object is the result of a merger of two gas-rich galaxies of unequal masses ($1/3 \lesssim m/M \lesssim 2/3$). At present, the current SB activity of Mrk 938 appears to be confined to a highly obscured central region of less than 1 kpc in size.

Fig. 3 presents the *Spitzer*/IRAC images at 3.6 and 8 μm. The 3.6-μm image, which probes the photospheric emission, shows the main body of the galaxy plus some extended low surface brightness emission. The north-east tidal tail of this merger system is clearly detected in the form of diffuse emission and some knots. There also exists a south-west tail with a much fainter optical surface brightness that is hardly seen in the 3.6-μm image. The knots in the north-east tail, also detected in the IRAC 8-μm image, appear to be coincident with the blue knots lying at a projected distance of ∼50 arcsec (∼21 kpc) from the nucleus (Schweizer & Seitzer 2007). Knots in both tidal tails are associated with H ii regions (A. Pérez-García, private communication).

The IRAC 8-μm emission, which probes dust continuum emission and PAH emission, is dominated by the presence of a bright central region. This region appears slightly resolved with a size (FWHM) of 2.3 arcsec (∼950 pc). The size of the 8-μm emitting region inferred from the IRAC data is in good agreement with the distribution of the mid-IR emission detected from ground-based

high angular resolution imaging as measured by Miles et al. (1996). These authors also showed that there are two mid-IR sources in the central regions of Mrk 938 separated 1.2 arcsec, although most of the mid-IR emission arises from a resolved source with an angular size of 1 arcsec (FWHM). This confirms that the SB region in this galaxy is only relatively compact (∼0.5–1 kpc, FWHM), as is the case in a large fraction of local LIRGs (Alonso-Herrero et al. 2006; Rujopakarn et al. 2011a). Also, the presence of extended mid-IR emission in the central regions of Mrk 938 is in agreement with the result that the AGN contribution to the mid-IR emission is low, as demonstrated in Section 3.2. We used PACS 70-μm and MIPS 24-μm images, which have comparable angular resolution, and probed the current star formation. We can set an upper limit to the SB region of ≤ 5 arcsec ∼ 2 kpc (FWHM), which is in good agreement with the measured size at shorter wavelengths.

We analysed the *Herschel* brightness profiles of Mrk 938 and compared them with those of point-like sources. We found no evidence of extended emission in any of the PACS or SPIRE bands. As a sanity check, we performed aperture photometry on the PACS 70-μm image using small radii, in this case 6 and 14 arcsec. After applying the corresponding aperture corrections, we obtained values in agreement with the integrated flux at 70 μm, therefore confirming that we are not detecting extended emission.

4.2 Star formation rate

Based on a variety of morphological, photometric and spectroscopic arguments, Schweizer & Seitzer (2007) concluded that the star formation activity of Mrk 938 was higher and more spread out in the past. As a result of the merger process, a galaxy-wide SB started about 600 Myr ago. It is this post-SB population that appears to dominate the emission from the blue disc present in this system. Riffel et al. (2008) used near-IR spectroscopy to study the stellar populations in the central region of this galaxy. They found that the near-IR emission of this galaxy is dominated by an intermediate-age stellar population of ∼1 Gyr, whereas the *young* (≤30 Myr) stellar population contributes to less than 25 per cent of this emission.

In the previous section we saw that most of the IR emission of Mrk 938 appears to be coming from a relatively compact region 0.5–2 kpc in size. In very dusty galaxies, as is the case of Mrk 938, this IR emission is probing the *current* SFR. This is because the UV light emitted by the young stars is absorbed by the dust and re-emitted in the IR. Therefore, some IR monochromatic luminosity or, alternatively, the total IR luminosity can be used to estimate the SFR (Kennicutt et al. 2009). The 24-μm monochromatic luminosity has been found to be a good indicator of the current SFR of dusty galaxies (e.g. Alonso-Herrero et al. 2006; Calzetti et al. 2007; Rieke et al. 2009). It has the advantage that it traces dust heated by the most massive stars, hence directly probing the *current* star formation activity. We used the Rieke et al. (2009) calibration:

$$\text{SFR}_{\text{IR}}\left(\text{M}_\odot\,\text{yr}^{-1}\right) = 7.8 \times 10^{-10} L_{24\,\mu\text{m}}\left(\text{L}_\odot\right)$$
$$\times \left\{7.76 \times 10^{-11} L_{24\,\mu\text{m}}\left(\text{L}_\odot\right)\right\}^{0.048}, \quad (1)$$

which assumes a Kroupa initial mass function (IMF).[5] Using $L_{24\,\mu\text{m}} = 5.3 \times 10^{10}\,\text{L}_\odot$ (calculated from the 24-μm flux in Table 1), we estimated a SFR_{IR} of 42 $\text{M}_\odot\,\text{yr}^{-1}$ to an accuracy within 0.2 dex (after removing the AGN contribution at this wavelength). This value is actually the *obscured* SFR. This value lies between the

values estimated by Vega et al. (2008) of 21 and 151 $\text{M}_\odot\,\text{yr}^{-1}$ based on SED fitting for star formation in the last 10 Myr and averaged over the entire burst, respectively. Also, our derived SFR is similar to the 64 $\text{M}_\odot\,\text{yr}^{-1}$ obtained from 1.4-GHz observations (Fernández et al. 2010).

As a sanity check we can test the above hypothesis that most of the ongoing SFR in LIRGs is taking place in obscured environments.

A source of uncertainty in the SFR calculation using IR indicators arises if a significant fraction of the stellar luminosity is not absorbed and then re-emitted in the IR, but escapes directly in the UV instead. We derived the SFR_{UV} using the far-UV flux for this galaxy. This was found by correlation of the source position with the *GALEX* archive. Taking into account a Galactic colour excess $E(B - V) = 0.027$ (quantity reported in NED[6]) and applying the extinction curve of Fitzpatrick (1999), we derived the UV-corrected flux ($F_{\text{UV}}^c = 0.62$ mJy). Following Kennicutt (1998), assuming a flat continuum and scaling to a Kroupa IMF, we have

$$\text{SFR}_{\text{UV}}\left(\text{M}_\odot\,\text{yr}^{-1}\right) = 9.2 \times 10^{-29} L_\nu\left(\text{erg s}^{-1}\,\text{Hz}^{-1}\right), \quad (2)$$

where L_ν is the UV luminosity. For Mrk 938 we find that the SFR_{UV} represents ∼3 per cent of the SFR_{IR}, as also found in Howell et al. (2010). This value is in agreement with the median value found for a sample of LIRGs in Buat et al. (2007) and Pereira-Santaella et al. (2011).

Similarly, we can estimate the *unobscured* SFR from the observed (not corrected for extinction) integrated Hα luminosity ($L_{\text{H}\alpha} = 10^{42}$ erg s^{-1}) reported by Moustakas & Kennicutt (2006). We used the SFR recipe of Kennicutt et al. (2009) that accounts for the *unobscured* and *obscured* SFR in terms of the Hα and 24-μm luminosities, respectively. We inferred that most (∼90–95 per cent) of the current star formation in Mrk 938 is *obscured*, and thus likely to be taking place in the compact SB region revealed by the mid-IR observations described above. This is in agreement with the small value found for the SFR_{UV} calculated above.

4.3 X-rays from star formation

For a SB, the emission of radiation in the X-ray domain can be attributed to a combination of components like supernova remnants, hot plasmas associated with star-forming regions and high-mass X-ray binaries within the galaxy among others (Fabbiano 1989). Several investigations have revealed correlation between the X-ray emission and total SFR in SBs (e.g. Ranalli, Comastri & Setti 2003; Pereira-Santaella et al. 2011). The linear relation of Pereira-Santaella et al. (2011) reads

$$\text{SFR}_{\text{IR+UV}}\left(\text{M}_\odot\,\text{yr}^{-1}\right) = \text{constant} \times 10^{-40} L_{\text{X}}\,\text{erg s}^{-1}\,\text{Hz}^{-1}, \quad (3)$$

with a 0.25 dex scatter, where constant = 3.4(± 0.3) and 3.9 (± 0.4) for the soft 0.5–2 keV and hard 2–10 keV X-rays, respectively. Applying this equation with the SFRs derived in Section 4.2, we estimate the following luminosities due to star formation activity in Mrk 938: $L_{0.5-2\,\text{keV}} = 1.2(\pm0.6) \times 10^{41}$ erg s^{-1} and $L_{2-10\,\text{keV}} = 1.0(\pm0.6) \times 10^{41}$ erg s^{-1}. The errors take into account the uncertainties in the SFR value and the uncertainties in equation (3).

We have compared the X-ray emission expected from star formation activity as calculated above with that of the fitted *XMM–Newton*

---

[5] Using a Salpeter IMF would result in a SFR approximately 1.4 times higher than that from the Kroupa IMF (see e.g. Kennicutt et al. 2009).

[6] The NASA/IPAC Extragalactic Database (NED) is operated by the Jet Propulsion Laboratory, California Institute of Technology, under contract with the National Aeronautics and Space Administration.

data. Using the luminosities measured in Section 2.3 for the best-fitting model to the X-ray data, we get a consistent value for the soft component ($0.5^{+0.2}_{-0.2} \times 10^{41}$ erg s^{-1}). This is in agreement with the fact that most, if not all, of the X-ray emission at soft energies is produced by the SB, as is also the case in a large fraction of local LIRGs (Pereira-Santaella et al. 2011). Also, the model derived from the fit of the X-ray data is consistent with star formation. However, in the 2–10 keV band, the luminosity of the X-ray fitting is an order of magnitude higher than that expected from the SFR. This was a priori anticipated because the AGN is the major contributor to the harder energies.

5 SPECTRAL ENERGY DISTRIBUTION AND DUST PROPERTIES

Several attempts have been made in the past to model the IR and submillimetre SED of LIRGs and ULIRGs using a modified black-body with one or several dust temperature or full radiative transfer modelling (see e.g. Dunne & Eales 2001; Klaas et al. 2001; Vega et al. 2008; Clements, Dunne & Eales 2010). Here we use for the first time *Herschel* photometry and data from the literature to obtain better estimates of the dust properties of Mrk 938. Table 1 presents our *Herschel* photometry as well as *IRAS*, *Spitzer* and *ISO* data compiled from the literature to construct the far-IR SED. The errors quoted for the *Herschel* flux densities take into account the photometric calibration uncertainties of ∼10 per cent in all the bands. The remaining errors listed in Table 1 are those given in the corresponding references.

We parametrized the SED of Mrk 938 using the standard modified blackbody, which depends on the dust temperature (T_{dust}) and the dust emissivity (β). In the case of optically thin emission in the IR, this function can be approximated as

$$f_\nu \propto \frac{\nu^{3+\beta}}{e^{h\nu/KT_{dust}} - 1}. \qquad (4)$$

We fixed $\beta = 2$, as it has been found to be a reasonable value for IR bright galaxies (Dunne & Eales 2001). Then we used a χ^2 minimization method to fit the dust temperature. The SED fit was

done using all the flux densities for $\lambda \geq 60\,\mu m$ given in Table 1, with the normalization at 100 μm. For the *IRAS* and *ISO* flux densities we used a 10 per cent uncertainty.

We obtained a best-fitting dust temperature of $T_{dust} = 36.5$ K. As can be seen from Fig. 6 (left-hand panel), using a single temperature produces a good fit to the far-IR SED of Mrk 938. Acceptable fits ($\chi^2 < 1.5 \times \chi^2_{min}$) were also obtained in the range of temperatures $T_{dust} = 36^{+4}_{-3}$ K (the fits for the limiting temperatures are shown in Fig. 6 as dotted lines). The best-fitting temperature is similar to those found by Klaas et al. (2001) for local (U)LIRGs using similar assumptions. We also tried a fit using $\beta = 1.5$, which has been found to fit better the SEDs of LIRGs and ULIRGs (Dunne & Eales 2001; Clements et al. 2010). The fit provided a higher dust temperature, as expected. However, this fit was considerably worse, having a value of χ^2 more than three times higher than that obtained with $\beta = 2$.

We derived the dust mass (M_{dust}) using the following equation (adapted from Hildebrand 1983):

$$M_{dust} = \frac{D_L^2 f_\nu}{\kappa_\nu B_\nu(T_{dust})}, \qquad (5)$$

where f_ν is the observed flux density, D_L is the luminosity distance, $B_\nu(T_{dust})$ is the blackbody emission for the best-fitting dust temperature and κ_ν is the absorption coefficient. We evaluated this expression at 250 μm using an absorption coefficient of $\kappa_{250\,\mu m} = 4.99$ cm^2 g^{-1} as interpolated from the dust model of Li & Draine (2001). We obtained $M_{dust} = 3 \times 10^7$ M$_\odot$, which is consistent with the values derived for local ULIRGs and other IR-bright galaxies (see Klaas et al. 2001; Clements et al. 2010, and references therein). For the range of acceptable dust temperatures, the inferred uncertainty in the calculated dust mass is ∼20 per cent. Vega et al. (2008) estimated an M_{dust} of 8.5×10^7 M$_\odot$. However, they used the dust-to-mass ratio as conversion factor between the gas and the dust mass, using a fixed value of 100 for all sources in their sample. This can introduce a large uncertainty in the dust mass. This is most probably the reason for the difference between our value and that in Vega et al. (2008).

We have also fitted the SED of LIRGs using a two-temperature model, similar to those used in other works (e.g. Dunne & Eales
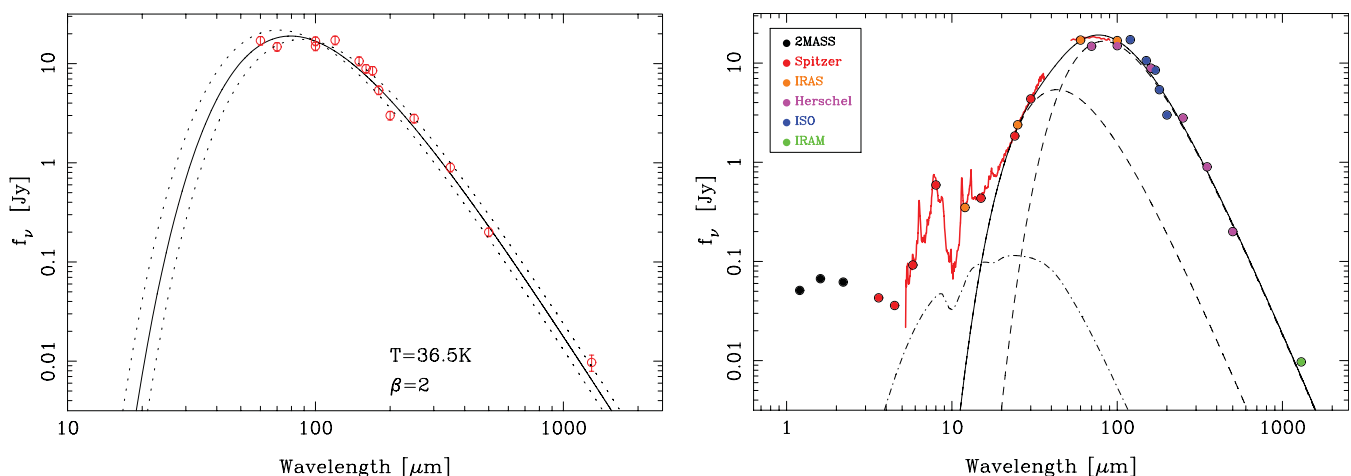

Figure 6. SEDs of Mrk 938. The left-hand panel shows the far-IR SED and the best fit (solid line) with a modified blackbody with fixed $\beta = 2$ and a best-fitting temperature of $T_{dust} = 36.5$ K. We also plotted acceptable fits (see text) as dotted lines, corresponding to $T_{dust} = 33$ K and $T_{dust} = 41$ K. The right-hand panel shows the full IR SED including all the photometric points in Table 1 (the colour code for the different instruments appears in the figure inset), as well as our extracted IRS spectrum and the MIPS-SED data of Gallimore et al. (2010) as red solid lines. We have also plotted our modelling to the mid- and far-IR data using two modified blackbodies (solid black line), with fixed $\beta = 2$ and best-fitting temperatures of $T^w_{dust} = 67$ K and $T^c_{dust} = 35$ K for the warm and cold components, respectively (dashed lines). The grey dot-dashed line is the fitted type 2 AGN template derived in Section 3.2.

2001; Clements et al. 2010), where we have taken into account all flux density values for $\lambda \geq 24\,\mu m$ to obtain a better constraint of the properties of the warm dust. Using two modified blackbody functions and $\beta = 2$, we obtained $T_{\mathrm{dust}}^{\mathrm{w}} = 67\,K$ and $T_{\mathrm{dust}}^{\mathrm{c}} = 35\,K$ for the warm and cold components, respectively. As expected, the temperature of the cold dust is very similar to that of the single blackbody fit. We also note that the temperature of the warm dust is not tightly constrained, as $T_{\mathrm{dust}}^{\mathrm{w}} = 67 \pm 5\,K$ produces values of χ^2 similar to χ_{min}^2. Finally, the goodness of the fit of the two temperature model is only marginally better than the single temperature fit. Clements et al. (2010) found higher dust temperatures for ULIRGs than those of lower luminosity systems, i.e. a median dust temperature of 42 K for a sample of ULIRGs, while a median of 35 K has been found for normal galaxies (Dunne & Eales 2001). The latter is consistent with the relatively cold temperature found in Mrk 938. We also find that the mass ratio of the cold to the warm dust component is very high ($M_{\mathrm{dust}}^{\mathrm{c}}/M_{\mathrm{dust}}^{\mathrm{w}} \sim 79$), which clearly indicates that the cold component is dominant in this galaxy. The total dust mass is very similar to the value obtained with one dust temperature.

In Fig. 6 (right-hand panel) we have plotted the entire SED including the torus model of *hot* dust and the best-fitting model to the far-IR data using the combination of two blackbodies described above. The latter best-fitting temperatures are typical of star-forming regions in the galaxy disc, therefore confirming that the active nucleus is not responsible for most of the observed dust emission (as seen in e.g. Hatziminaoglou et al. 2010). Dust in regions of star formation have peak temperatures between 40 and 70 K, while radiation of AGN origin has a characteristic peak temperature within the range 120–170 K (e.g. Pérez García & Rodríguez Espinosa 2001). This is in agreement with what we found in Section 3.2 from the spectral decomposition, where we concluded that the dusty torus only contributes up to 2 per cent of the observed IR emission.

As a comparison, Ramos Almeida et al. (2011b) studied the dust distribution of the Seyfert 2 galaxy NGC 3081 also including *Herschel* PACS and SPIRE data in their analysis. The nuclear emission of this galaxy was reproduced by a clumpy torus model of warm dust heated by the AGN. The circumnuclear emission was fitted by a cold dust component at 28 K heated by young stars in the galaxy disc, plus a colder component at 19 K in the outskirts of the galaxy heated by the interstellar radiation. Similarly, Radovich

et al. (1999) decomposed the SED of the narrow-line galaxy NGC 7582 and found an extranuclear emission dominated by cold dust at 30 K, plus an additional very cold component emitting at 17 K. We do not detect this very cold dust component in Mrk 938. This is because we cannot resolve any extended emission in our data, and although this component is likely to exist its contribution to the total IR luminosity is negligible.

We can finally estimate the size of the IR-emitting region. Following Klaas et al. (2001), for an optically thin (transparent) blackbody with $\beta = 2$, the far-IR emitting component is homogeneously distributed in a 'minimum face-on disc' of radius r_τ with the form:

$$r_\tau(\mathrm{pc}) = \left(\frac{M_{\mathrm{dust}}/M_\odot}{41.7\pi\tau_{100\,\mu m}} \right)^{0.5}. \tag{6}$$

Assuming an opacity at $100\,\mu m$ $\tau_{100\,\mu m} \sim 0.5$–1, we obtain a minimum radius for the IR-emitting region of $r_\tau \sim 500$–800 pc, in good agreement with our measurements from the mid-IR images in Section (4.1).

6 SUMMARY AND CONCLUSIONS

LIRGs have emerged as an important cosmological class given that they may play a central role in our understanding of the general evolution of galaxies and black holes. We have studied Mrk 938, a LIRG in the local Universe classified as a Seyfert 2 through optical spectroscopy. Table 4 summarizes the relevant parameters resulting from the present work which, in addition to table 8 in Schweizer & Seitzer (2007), shows the main properties of Mrk 938. The analysis of the X-ray data favours the presence of a highly obscured AGN, where the SB emission prevails at soft energies and the active nucleus dominates at hard energies. The absorption-corrected hard X-ray luminosity is too high to be originated only in a pure SB.

We have performed a decomposition of the *Spitzer*/IRS spectrum and recovered the AGN contribution to the IR luminosity, which is overwhelmed by the intense emission of star formation. The best-fitting model to the IRS data was achieved with a combination of a type 2 AGN plus a $10^{12}\,L_\odot$ SB templates. Using the derived fractional contribution of the AGN to the luminosity at $24\,\mu m$, we derived an AGN bolometric contribution to the IR luminosity

Table 4. Summary of the properties of Mrk 938 derived in this paper.

AGN Properties			
Hard X-ray luminosity	$L_{2-10\mathrm{keV}}$	$1.4^{+0.4}_{-0.2} \times 10^{42}$ erg s^{-1}	Absorption corrected
Bolometric luminosity	$L_{\mathrm{bol}}(\mathrm{AGN})$	$1.6^{+1.1}_{-0.6} \times 10^{43}$ erg s^{-1}	From X-ray and bolometric correction
		$2.6^{+2.6}_{-1.3} \times 10^{43}$ erg s^{-1}	From IRS decomposition
AGN contribution	Bolometric	2^{+2}_{-1} per cent	From IRS decomposition
	0.5–2 keV	≤ 5 per cent	From comparison with X-ray luminosity due to star formation
	2–10 keV	≥ 85 per cent	From comparison with X-ray luminosity due to star formation
	$24\,\mu m$	5 (± 3) per cent	From IRS decomposition
SB Properties			
SFR	$\mathrm{SFR}_{\mathrm{obscured}}$	$42\,M_\odot\,\mathrm{yr}^{-1}$	From MIPS $24\,\mu m$, Kroupa IMF
Size IR emitting region	d_{IR}	$\sim 1\,\mathrm{kpc}$	From IRAC $8\,\mu m$ (FWHM)
		$\leq 2\,\mathrm{kpc}$	From MIPS $24\,\mu m$, PACS $70\,\mu m$ (FWHM)
		$1 - 1.6\,\mathrm{kpc}$	From dust mass, assuming $\tau_{100\,\mu m} = 0.5$–1
Dust temperature	$T_{\mathrm{dust}}^{\mathrm{c}}$	35 (± 4) K	Two-temperature fit, fixed $\beta = 2$
	$T_{\mathrm{dust}}^{\mathrm{w}}$	63 (± 4) K	Two-temperature fit, fixed $\beta = 2$
Dust mass	M_{dust}	$3 (\pm 1) \times 10^7\,M_\odot$	Two-temperature fit, fixed $\beta = 2$
Dust mass ratio	$M_{\mathrm{dust}}^{\mathrm{c}}/M_{\mathrm{dust}}^{\mathrm{w}}$	79	Two-temperature fit, fixed $\beta = 2$

of ∼2 per cent, which is in agreement with previous estimations. This supports the proposed scenario that intense dusty SBs are responsible for the high IR luminosities in most local LIRGs. The analysis of IR images shows that the IR emission of Mrk 938 originates in a relatively compact region, with a size between 0.5 and 2 kpc. We have also demonstrated that most of the ongoing SFR is produced in an obscured environment as expected for LIRGs.

The wealth of multiwavelength archival data of this source has been used in conjunction with our own observations to constrain the SED. We have used *Herschel* imaging data for the first time to constrain the cold dust emission with unprecedented accuracy. We have derived dust temperatures of 63 and 35 K for the warm and cold components, respectively. Using the results of our SED fitting we have derived a cold dust mass of 3×10^7, $M_\odot$ and a very high mass ratio of the cold to the warm dust components. This demonstrates that emission of cold dust clearly dominates the IR SED.

ACKNOWLEDGMENTS

REFERENCES

Albrecht M., Krügel E., Chini R., 2007, A&A, 462, 575
Alonso-Herrero A., Rieke G. H., Rieke M. J., Colina L., Pérez-González P. G., Ryder S. D., 2006, ApJ, 650, 835
Alonso-Herrero A., Pereira-Santaella M., Rieke G. H., Rigopoulou D., 2012, ApJ, 744, 2
Arnouts S. et al., 2007, A&A, 476, 137
Asensio Ramos A., Ramos Almeida C., 2009, ApJ, 696, 2075
Barthelmy S. D. et al., 2005, Space Sci. Rev., 120, 143
Bassani L., Dadina M., Maiolino R., Salvati M., Risaliti G., della Ceca R., Matt G., Zamorani G., 1999, ApJS, 121, 473
Bernard-Salas J. et al., 2009, ApJS, 184, 230
Brandl B. R. et al., 2006, ApJ, 653, 1129
Buat V., Marcillac D., Burgarella D., Le Floc'h E., Takeuchi T. T., Iglesias-Páramo J., Xu C. K., 2007, A&A, 469, 19
Calzetti D. et al., 2007, ApJ, 666, 870
Chanial P., Flores H., Guiderdoni B., Elbaz D., Hammer F., Vigroux L., 2007, A&A, 462, 81
Clements D. L., Dunne L., Eales S., 2010, MNRAS, 403, 274
Dale D. A., Helou G., 2002, ApJ, 576, 159
Deo R. P., Crenshaw D. M., Kraemer S. B., Dietrich M., Elitzur M., Teplitz H., Turner T. J., 2007, ApJ, 671, 124
Deo R. P., Richards G. T., Crenshaw D. M., Kraemer S. B., 2009, ApJ, 705, 14
Dickey J. M., Lockman F. J., 1990, ARA&A, 28, 215
Dunne L., Eales S. A., 2001, MNRAS, 327, 697
Elbaz D., Cesarsky C. J., Chanial P., Aussel H., Franceschini A., Fadda D., Chary R. R., 2002, A&A, 384, 848
Fabbiano G., 1989, ARA&A, 27, 87
Fazio G. G. et al., 2004, ApJS, 154, 10
Fernández X., van Gorkom J. H., Schweizer F., Barnes J. E., 2010, AJ, 140, 1965
Ferrarese L., Ford H., 2005, A&A, 116, 523
Fitzpatrick E. L., 1999, PASP, 111, 63
Gabriel C. et al., 2004, in Ochsenbein F., Allen M. G., Egret D., eds, ASP Conf. Ser. Vol. 314, Astronomical Data Analysis Software and Systems (ADASS) XIII. Astron. Soc. Pac., San Francisco, p. 759
Gallimore J. F. et al., 2010, ApJS, 187, 172
Genzel R. et al., 1998, ApJ, 498, 579
Gonçalves A. C., Véron-Cetty M.-P., Véron P., 1999, A&AS, 135, 437
Griffin M. J. et al., 2010, A&A, 518, L3
Guainazzi M., Matt G., Perola G. C., 2005, A&A, 444, 119
Hatziminaoglou E. et al., 2010, A&A, 518, L33
Hildebrand R. H., 1983, Q. J. R. Astron. Soc., 24, 267
Hopkins P. F., Hernquist L., Cox T. J., Di Matteo T., Robertson B., Springel V., 2006, ApJS, 163, 1
Houck J. R. et al., 2004, ApJS, 154, 18
Howell J. H. et al., 2010, ApJ, 715, 572
Jarrett T. H., Chester T., Cutri R., Schneider S. E., Huchra J. P., 2003, AJ, 125, 525
Kennicutt R. C., Jr, 1998, ARA&A, 36, 189
Kennicutt R. C., Jr et al., 2009, ApJ, 703, 1672
Klaas U. et al., 2001, A&A, 379, 823
Kormendy J., Richstone D., 1995, ARA&A, 33, 581
La Franca F. et al., 2005, ApJ, 635, 864
Le Floc'h E. et al., 2005, ApJ, 632, 169
Li A., Draine B. T., 2001, ApJ, 554, 778
Magdziarz P., Zdziarski A. A., 1995, MNRAS, 273, 837
Maiolino R., Salvati M., Bassani L., Dadina M., della Ceca R., Matt G., Risaliti G., Zamorani G., 1998, A&A, 338, 781
Marconi A., Hunt L. K., 2003, ApJ, 589, L21
Marconi A., Risaliti G., Gilli R., Hunt L. K., Maiolino R., Salvati M., 2004, MNRAS, 351, 169
Matt G., Brandt W. N., Fabian A. C., 1996, MNRAS, 280, 823
Menéndez-Delmestre K. et al., 2009, ApJ, 699, 667
Miles J. W., Houck J. R., Hayward T. L., Ashby M. L. N., 1996, ApJ, 465, 191
Moustakas J., Kennicutt R. C., Jr, 2006, ApJS, 164, 81
Mullaney J. R., Alexander D. M., Goulding A. D., Hickox R. C., 2011, MNRAS, 414, 1082
Müller T., Nielbock M., Balog Z., Klaas U., Vilenius E., 2011, PACS Photometer - Point-Source Flux Calibration, PICC-ME-TN-037 v1.0

Nardini E., Risaliti G., Salvati M., Sani E., lmanishi M., Marconi A., Maiolino R., 2008, MNRAS, 385, L130

Nardini E., Risaliti G., Watabe Y., Salvati M., Sani E., 2010, MNRAS, 405, 2505

Nenkova M., Sirocky M. M., Ivezić Ž., Elitzur M., 2008a, ApJ, 685, 147

Nenkova M., Sirocky M. M., Nikutta R., Ivezić Ž., Elitzur M., 2008b, ApJ, 685, 160

Pereira-Santaella M., Alonso-Herrero A., Rieke G. H., Colina L., Díaz-Santos, T., Smith J.-D. T., Pérez-González P. G., Engelbracht C. W., 2010a, ApJS, 188, 447

Pereira-Santaella M., Diamond-Stanic A. M., Alonso-Herrero A., Rieke G. H., 2010b, ApJ, 725, 2270

Pereira-Santaella M. et al., 2011, A&A, in press (arXiv:1109.0921)

Pérez García A. M., Rodríguez Espinosa J. M., 2001, ApJ, 557, 39

Pérez-González P. G. et al., 2005, ApJ, 630, 82

Petric A. O. et al., 2011, ApJ, 730, 28

Pilbratt G. L. et al., 2010, A&A, 518, L1

Poglitsch A. et al., 2010, A&A, 518, L2

Polletta M., Bassani L., Malaguti G., Palumbo G. G. C., Caroli E., 1996, ApJS, 106, 399

Radovich M., Klaas U., Acosta-Pulido J., Lemke D., 1999, A&A, 348, 705

Ramos Almeida C. et al., 2011a, ApJ, 731, 92

Ramos Almeida C. et al., 2011b, MNRAS, 417, L46

Ranalli P., Comastri A., Setti G., 2003, A&A, 399, 39

Rieke G. H., Alonso-Herrero A., Weiner B. J., Pérez-González P. G., Blaylock M., Donley J. L., Marcillac D., 2004, ApJS, 154, 25

Rieke G. H., Alonso-Herrero A., Weiner B. J., Pérez-González P. G., Blaylock M., Donley J. L., Marcillac D., 2009, ApJ, 692, 556

Riffel R., Pastoriza M. G., Rodríguez-Ardila A., Maraston C., 2008, MNRAS, 388, 803

Rujopakarn W., Rieke G. H., Eisenstein D. J., Juneau S., 2011a, ApJ, 726, 93

Rujopakarn W., Rieke G. H., Weiner B. J., Rex M., Walth G. L., Kartaltepe, J. S., 2011b, preprint (arXiv:1107.2921)

Sanders D. B., Mirabel I. F., 1996, ARA&A, 34, 749

Sanders D. B., Mazzarella J. M., Kim D.-C., Surace J. A., Soifer B. T., 2003, AJ, 126, 1607

Schweizer F., Seitzer P., 2007, AJ, 133, 2132

Smith J. D. T. et al., 2007, PASP, 119, 1133

Spinoglio L., Andreani P., Malkan M. A., 2002, ApJ, 572, 105

Spoon H. W. W., Marshall J. A., Houck J. R., Elitzur M., Hao L., Armus L., Brandl B. R., Charmandaris V., 2007, ApJ, 654, L49

Tommasin S., Spinoglio L., Malkan M. A., Fazio G., 2010, ApJ, 709, 1257

Vega O., Clemens M. S., Bressan A., Granato G. L., Silva L., Panuzzo P., 2008, A&A, 484, 631

Veilleux S., Kim D.-C., Sanders D. B., Mazzarella J. M., Soifer B. T., 1995, ApJS, 98, 171

Yuan T.-T., Kewley L. J., Sanders D. B., 2010, ApJ, 709, 884

This paper has been typeset from a TEX/LATEX file prepared by the author.